Size-dependent effect of ion bombardment on Au nanoparticles on top of various substrates: Thermodynamically dominated capillary forces versus sputtering

A. Klimmer* and P. Ziemann†
Institute of Solid State Physics, Ulm University, 89069 Ulm, Germany

J. Biskupek and U. Kaiser
Electron Microscopy Group, Ulm University, 89069 Ulm, Germany

M. Flesch*

(Received 22 January 2009; published 16 April 2009)

Hexagonally ordered arrays of Au nanoparticles exhibiting narrow size distributions were prepared on top of Si wafers with either a thin native oxide or a thick thermally oxidized layer as well as on top of crystalline (0001)-oriented sapphire substrates. Subsequent irradiation of these nanoparticles by 200 keV Ar^+ and Xe^+, respectively, in combination with transmission electron microscopy analysis (TEM) corroborated the previously reported phenomenon of bombardment-induced burrowing of metallic nanoparticles into SiO_x while conserving their spherical shape [X. Hu *et al.*, J. Appl. Phys. **92**, 3995 (2002)]. Performing the ion irradiations on particle ensembles of different radii R_0 ($1.3\ \text{nm} \leq R_0 \leq 5.3\ \text{nm}$) and determining the burrowing effect by atomic force microscopy combined with TEM provide sufficient statistics to allow a quantitative description of this effect. In addition to the thermodynamic driving forces necessary for the burrowing effect, sputtering of the nanoparticles due to the ion bombardment has to be included to arrive at an excellent theoretical description of the experimental data. The magnitude of sputtering can be quantified for the Au/sapphire system, where the burrowing effect is found to be completely suppressed. In that case, the theoretical description can even be improved by assuming a size-dependent sputtering coefficient for the Au nanoparticles. Combining this type of sputtering with the thermodynamically driven burrowing effect delivers a consistent model for all ion bombarded Au nanoparticles on top of SiO_x. Specifically, the residual heights of the Ar^+- or Xe^+-induced burrowing of Au nanoparticles can be scaled on top of each other if plotted versus the average displacements per target atom rather than versus the applied ion fluences.

DOI: 10.1103/PhysRevB.79.155427 PACS number(s): 61.46.−w, 61.80.Jh, 61.82.Bg

I. INTRODUCTION

Ion implantation and irradiation are two well-established variants of bombarding a solid in order to incorporate additional atomic species or to exclusively create structural disorder, respectively. For example, in semiconductor technology, ion implantation is one of the standard methods applied for doping, which offers additional control over the depth distribution of dopants by properly adjusting the energy of the incoming ions while their lateral distribution can be defined by lithographically opened windows.[1] Since in the following the ion energies are restricted to values below 300 keV, a range typical of research implanters, the corresponding projected ion ranges are restricted as well to values of some tens up to some hundred nanometers depending on the specific ion-target combination. As opposed to implantation, ion irradiation aims at producing radiation damage without incorporating the related projectiles. Thus, in the ideal case, the thickness of a sample subjected to irradiation should be significantly smaller than the projected range of the applied ions. As a consequence of the above energy restriction, standard ion irradiation experiments have to be performed on thin films.

From a physics point of view, both variants of ion bombardment helped to address questions related to the formation of metastable phases such as supersaturated solutions or amorphous metallic systems and to the influence of structural disorder on physical properties such as the superconducting, magnetic, or optical behavior of solids just to name a few.[2] The same type of questions arises again in the context of nanostructures. For instance, it is not at all clear whether nanostructures can be doped by implantation after their preparation or which type of bombardment-induced structural disorder will be stable. Especially, such questions are still open for semiconducting and metallic nanoparticles with diameters below 20 nm. While ion bombardment recipes have been developed to fabricate nanoparticles embedded in insulating, semiconducting, or metallic matrices,[3–6] ion irradiations of well-defined nanoparticles deposited on top of a given substrate are still scarce. Here, well-defined refers to ensembles exhibiting narrow size distributions of the particle size as well as of the interparticle distance. In that field of preparing nanoparticles along various chemical routes significant progress has been achieved recently,[7–9] aiming at fine tuning especially their optical and magnetic properties.[10,11] In the present contribution, one such route based on a micellar approach[12,13] is applied in order to fabricate hexagonally ordered arrays of Au nanoparticles on top of various substrates such as Si, SiO_2, and sapphire. As will be demonstrated, these particles forming the starting point of subsequent ion irradiation experiments exhibit narrow size distributions within a diameter range between 2.5 and 10.6 nm. The necessity for a narrow size distribution follows from the fact that the ion bombardment is genuinely a statistical

process demanding a large number of possibly identical objects to extract quantitative conclusions on irradiation-induced size changes. The above-mentioned hexagonal order of our ensembles additionally helps to redetect and identify particles after their bombardment.

Given such well-defined nanoparticle ensembles, what phenomena can be expected due to their ion irradiation? At least two extreme cases come to mind: first, complete destruction of nanoparticles due to spike events and, second, ion-induced burrowing of the particles while completely conserving their spherical shape. In the first scenario, when the projectile is hitting a target atom within a nanoparticle, this primary collision triggers an avalanche of moving target atoms by secondary knock-on events. The resulting liquidlike nonequilibrium state, which is confined to some nanometers depending in detail on the average transferred energies, exhibits typical lifetimes of the order of 10^{-14} s and is often referred to as energy spike or, less correct, as thermal spike. As a consequence of the comparable size of a spike and a nanoparticle volume, one might expect a spike-induced complete decomposition of nanoparticles. Indeed, in molecular-dynamics simulations of ion bombardments such spikes and related destructions of bombarded nanoparticles have been observed.[14] In the second scenario, thermodynamic driving forces resulting from different surface energies of the particle and its substrate in relation to their particle-substrate interface energy can lead to a burrowing of the particles if the ion bombardment is providing the necessary kinetic conditions. These conditions can be expressed in terms of an effective ion-induced viscosity of the substrate. Clearly, such an effect hinges on the proper choice of the particle-substrate combination. In a previous paper on burrowing Pt nanoparticles in SiO_2 this effect was experimentally studied by transmission electron microscopy (TEM) and a first model based on surface energy considerations was given.[15] Moreover burrowing of Au particles in SiO_2 and Si as a result of extensive electron-beam irradiation followed by additional heat treatment was directly observed *in situ* in a TEM.[16]

It is the focus of the present contribution to extend the database of this effect in order to test the above thermodynamic model quantitatively. However, in addition to ion-induced burrowing of particles, conventional sputter erosion may occur leading to a decrease of particle diameters, which, in turn, enhances the capillary forces leading to the burrowing effect. As will be demonstrated, this feedback, which was not considered, yet, in the previous model, does play a role and can experimentally be observed. One step further, the possibility of a size-dependent sputtering coefficient as discussed theoretically for nanoscaled spherical targets[17] will be addressed in the present experiments. Finally, once the nanoparticles are completely embedded within an underlying substrate, where they are insoluble under equilibrium conditions, the question arises as to the possibility of forcing them into metastable solid solution by a further ion bombardment.

II. EXPERIMENTAL

The present work is based on the significant progress with respect to the preparation of arrays of nanoparticles exhibiting narrow size distributions. In the following, exclusively Au nanoparticles will be studied prepared along a micellar route exploiting the self-organization of metal salt loaded inverse micelles which form in an apolar solvent such as toluene from diblock copolymers. Since this method has been described in detail previously,[12,13] here only a brief summary is given.

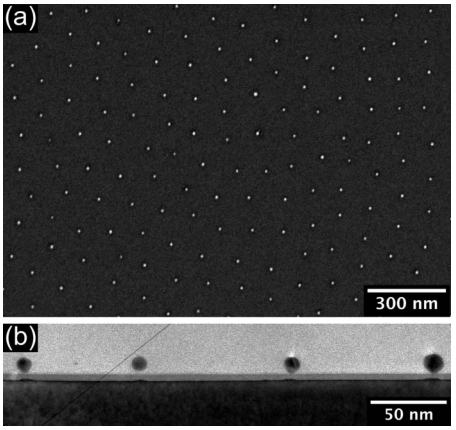

FIG. 1. Au nanoparticles (diameter 10.3 nm) prepared by a micellar approach on top of Si: (a) top view SEM image (30 kV, SE-detector) (b) bright-field TEM image (cross-sectional view).

The first step consists of depositing one layer of spherical reverse micelles produced when dissolving the commercially available diblock copolymer poly(styrene) $[m]$-block-poly(2-vinylpyridine) $[n]$(PS $[m]$-b-P2VP $[n]$) in toluene. In that case, the hydrophilic poly-2–vinylpyridine (P2VP) forms the core of the micelles and the hydrophobic polystyrene (PS) their outer corona. The integers n and m above indicate the number of monomers per block and, thus, determine the size of the resulting micelles. The core region can be selectively loaded with the Au salt $HAuCl_4$ serving as a precursor for Au nanoparticles. It turns out that on dip coating a substrate in an optimized way with the toluene solution containing the spherical micelles, they will self-assemble into a hexagonally ordered array. In the next step, by exposing this array to an isotropic oxygen plasma, the polymer matrix is completely removed and, in parallel, the precursor salt is transformed into metallic Au particles while the overall hexagonal order of their arrangement is conserved. This micellar approach allows control of both the interparticle distance and the particle size. While the former is primarily determined by the length of each polymer block with additional influence of the substrate velocity during the dip coating process,[18] the latter is related to the loading ratio L_{Au}, i.e., the ratio of ligated Au within the micellar core to the total number of pyridine moieties. As a result, particle diameters can be varied between 1 and 12 nm and interparticle distances between 20 and 140 nm. An example of a finally obtained array of Au nanoparticles (average diameter 10.3 nm) on top of a Si wafer is given in Fig. 1, where panel (a) shows a top view image as taken by scanning electron microscopy (SEM) and panel (b) a cross section taken by TEM. The following features are worth noting: (1) the immediately visible impression of equally sized nanospheres, which will be quantified below by fitting Gaussians to the

corresponding distributions revealing the related variances; (2) the high degree of hexagonal order of the Au nanoparticles with an average interparticle distance of 80 nm; and (3) a SiO_2 interlayer between the Si substrate and the nanoparticles, which, due to the above-mentioned oxygen plasma step, is thicker than corresponding native oxide layers, but still smaller than the size of the Au particles on top. Three types of substrates were applied: (001)-oriented Si wafers (*n* doped, 1–10 Ω cm) with a surface oxide of a somewhat enhanced thickness (typically 6–7 nm) as compared to native SiO_x, Si wafers with a thick (600 nm and 1000 nm) SiO_2 layer on top prepared by thermal oxidation, and (0001)-oriented sapphire.

To characterize the as-prepared particle arrays, atomic force microscopy (AFM) measurements as well as SEM and TEM investigations were performed. For this purpose, corresponding commercial instruments by Veeco [DI MultiMode AFM in combination with the analysis software WSXM (Ref. 19)], electron microscopes from Hitachi (S-5200, cold field-emission SEM) and Philips (CM 20, 200 kV TEM) were applied, respectively. While for AFM and SEM no additional surface treatments were needed, TEM investigations of cross-sectional samples demanded a special treatment. The samples were cut into stripes, glued face to face, and embedded into a 3 mm Ti grid. Then these sandwiches were ground, dimpled, and polished down to a thickness of about 5 μm. Low angle argon-ion etching (2 to 5 keV) was finally applied until electron transparency had been reached (sample thickness <100 nm). Since, in contrast to Si or SiO_x substrates, nanoparticles do not stick very well on sapphire surfaces, a thin film of SiO_x had to be deposited onto these samples prior to the mechanical treatment during TEM sample preparation to cover the nanoparticles and thus avoid unwanted damage.

III. RESULTS AND DISCUSSION

A. Au nanoparticles on top of silicon irradiated with 200 keV Ar^+: TEM results

To demonstrate the central phenomenon of the present study, we start with presenting the TEM results as obtained after ion irradiating (200 keV Ar^+) an array of Au nanoparticles (diameter 10.3 nm, interparticle distance 80 nm) on top of Si (as mentioned before, the thickness of the native oxide is enhanced to 6–7 nm due to the oxygen plasma step during the particle preparation). Corresponding high-resolution (HR) TEM images are shown in Fig. 2 for different ion fluences, as given in the caption. Three fluence ranges, which generally depend on the starting size of the particles, can clearly be distinguished. Below 10^{15} ions/cm^2 the nanoparticles appear unchanged with respect to their position on top of the thin oxide layer as well as with respect to their size and shape. For larger fluences, but below 5×10^{15} ions/cm^2, however, the nanoparticles apparently sink into the oxide layer [panels (b′), (c), and (c′)] and even at least partly into the underlying Si substrate [panel (b)] due to the ion irradiation while approximately conserving their spherical shape. For still higher ion fluences the nanoparticles finally can be forced into metastable solution within the Si substrate [panel (d)]. It is the shape conserving ion-induced burrowing of the Au nanoparticles into the substrate—previously reported for Pt nanoparticles on top of SiO_2 substrates[15]—which is at the focus of the present study. The TEM images of Fig. 2, however, also demonstrate a basic problem. Though providing principal evidence for the above surprising phenomenon, due to the statistical nature of the ion bombardment, individual nanoparticles exhibit a broad variance of the already buried height even at a given fixed ion fluence. Thus, for a quantitative analysis of the burrowing process, TEM must be supported by a measurement technique allowing for much better statistics. For this purpose, AFM tapping mode measurements were employed delivering the particle height averaged over a large array of particles with a narrow size distribution prior to the ion bombardment.

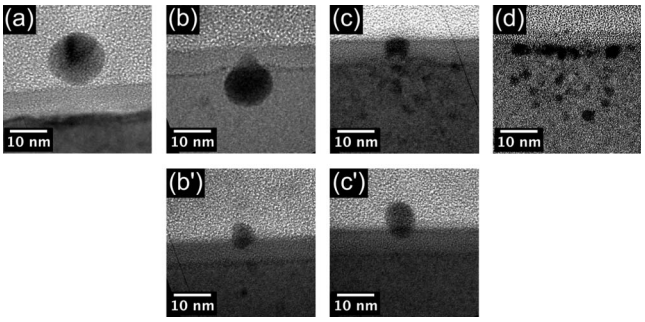

FIG. 2. (HR)TEM cross-section images of Au nanoparticles (diameter 10.3 nm) on top of Si and irradiated with 200 keV Ar^+ ions for various fluences: (a) 0.7×10^{15} ions/cm^2, (b)/(b′) 1.7×10^{15} ions/cm^2, (c)/(c′) 2.6×10^{15} ions/cm^2, and (d) 7.4×10^{15} ions/cm^2. Double panels such as (b) and (b′) demonstrate the statistical scatter of particle behavior at identical ion fluences.

B. Au nanoparticles on top of silicon oxide irradiated with 200 keV Ar^+: AFM and TEM results

As the TEM data above as well as the previous report on Pt nanoparticles[15] indicated that specific properties of SiO_2 may play a significant role in the ion-induced particle burrowing, the following AFM data were obtained for Au nanoparticles on top of thick SiO_2 layers prepared by thermal oxidation of Si. The experimental procedure is demonstrated in Fig. 3. Usually four AFM images such as the one shown in panel (a) were taken delivering height histograms including typically a couple of hundred nanoparticles, which then could be least-squares fitted to Gaussians [solid curves in panel (b)]. Clearly, the average particle height $\langle h\rangle$ as determined by AFM monotonously decreases due to ion bombardment accompanied by a corresponding decrease of the standard deviations σ. It should be noted, however, that the relative spread $\langle h\rangle/2\sigma$ is enhanced from 17% before irradiation to 42% after the highest ion fluence. Though the observed height decrease is in accordance with a burrowing effect demonstrated above for Si substrates, for the present SiO_2 case such an ion-induced burrowing still has to be corroborated. The corresponding evidence is provided by the TEM images presented in Fig. 4, where for increasing Ar^+

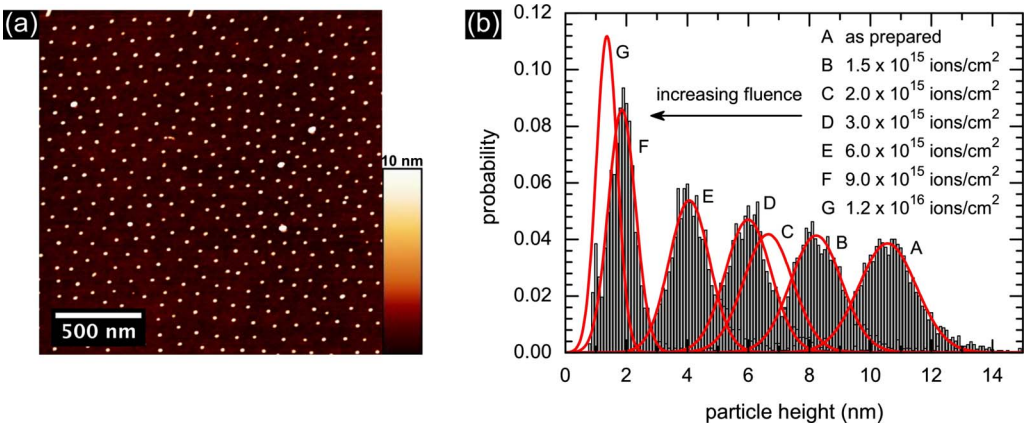

FIG. 3. (Color online) (a) AFM image of Au nanoparticles (diameter 10.6 nm) on top of SiO_2. (b) Size distributions of as-prepared and Ar^+-irradiated Au nanoparticles (200 keV, fluences as given in the inset). Solid curves are fits to Gaussians.

fluences different stages of burrowing including complete coverage can be seen. These images also suggest that the still visible height h of a particle above the substrate is related to the already buried part z of the diameter $2R$ by the simple relation $z=2R-h$, which will be assumed in the analysis below.

C. Au nanoparticles on top of silicon oxide irradiated with 200 keV Ar^+: Theory

In their seminal paper Hu *et al.*[15] attributed the ion-induced burrowing of nanoparticles to capillary forces acting on a solid particle on top of a viscous medium, where the viscosity η of the substrate is locally enhanced due to the ion bombardment despite nominally kept at ambient temperature. As discussed in Ref. 20, spike effects as well as point-defect-like entities may mediate the viscous flow in amorphous substrates. In both cases, however, the driving force for burying a solid spherical particle of radius R is thermodynamically related to its surface energy γ_p, to the surface energy of the viscous substrate γ_s, as well as to the corresponding interface energy $\gamma_{p,s}$. Accordingly, in Ref. 15 the problem is parameterized by the two quantities

$$a = \frac{\gamma_s + \gamma_p - \gamma_{p,s}}{\gamma_s} = 1 + \cos\,\vartheta \tag{1}$$

and

$$b = \frac{2\gamma_s}{3\eta}. \tag{2}$$

Expression (1), often addressed as Young's equation, relates the surface and interface energies to the wetting angle ϑ between the viscous substrate and the solid particle. The wetting behavior as expected for various values of the parameter a is sketched in Fig. 5 comprising again all situation from complete dewetting for $a=0$ to complete wetting for $a=2$. Thus, comparison to Fig. 4(c) showing an almost completely covered Au nanoparticle in SiO_2 after ion irradiation suggests a value of a close to 2. Referring to the coordinates h and z, respectively, as given in Fig. 5(b), Hu *et al.*[15] found for the velocity

$$\frac{dz}{dt} = b\frac{aR - z}{z}, \tag{3}$$

which transforms into

$$\frac{dh}{dt} = b\frac{h + (a-2)R}{h - 2R}, \tag{4}$$

as measurable by AFM. Following Hu *et al.*[15] further, the standard viscosity η is substituted by an ion-induced viscosity η_r and scaled by the ion flux $d\phi/dt$,

$$\eta = \eta_r\left(\frac{d\phi}{dt}\right)^{-1}. \tag{5}$$

In this way, one arrives at

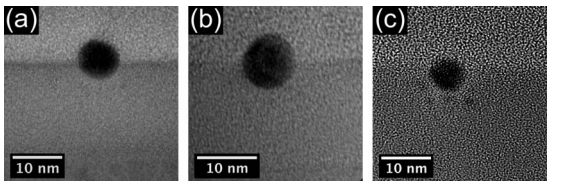

FIG. 4. (HR)TEM cross section for Au particles (diameter 10.6 nm) on top of SiO_2 after 200 keV Ar^+ irradiation (a) 1.7×10^{15} ions/cm^2, (b) 3.7×10^{15} ions/cm^2, and (c) 4.2×10^{15} ions/cm^2.

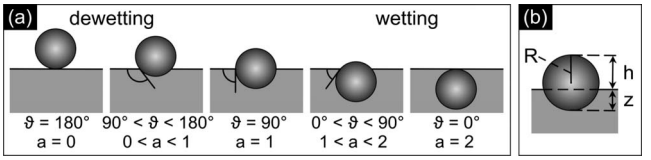

FIG. 5. (a) Schematics of final equilibrium positions of solid spheres sinking into a viscous substrate depending on the wetting conditions as expressed by the parameter a defined in Eq. (1). (b) Definition of the two lengths z and h used in the theoretical description.

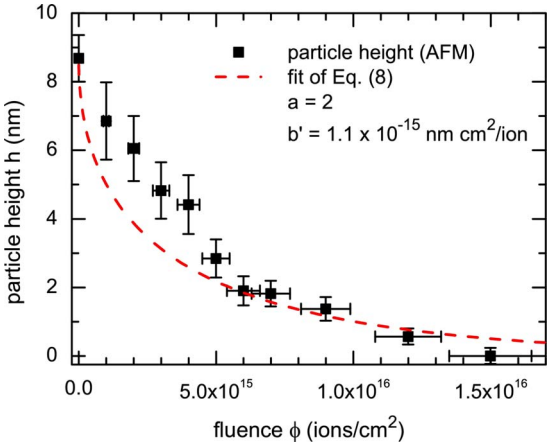

FIG. 6. (Color online) Decrease of the height of Au nanoparticles (starting diameter 8.8 nm) due to irradiation-induced burrowing by 200 keV Ar^+ ion. Closed squares are experimental data and dashed curve is a fit to Eq. (8) resulting in the parameters given in the inset.

$$\frac{dh}{d\phi} = b' \frac{h + (a-2)R}{h - 2R} \tag{6}$$

and

$$b' = \frac{2\gamma_s}{3\eta_r}. \tag{7}$$

Finally, separating the variables h and ϕ allows an analytical integration revealing

$$\phi(h) = \frac{h - 2R}{b'} - \frac{aR}{b'} \ln\left(\frac{h - 2R}{aR} + 1\right). \tag{8}$$

Treating a and b' as parameters, Eq. (8) was fitted to the experimental $h(\phi)$ data as obtained by AFM for a particle ensemble of starting diameter 8.8 nm. The result is presented in Fig. 6 demonstrating that the general trend is satisfactorily described by the above approach in agreement with the previously reported case of irradiated Pt nanoparticles on SiO_2.[15] From fitting the values $a=2$ and $b'=1.1 \times 10^{-15}$ nm cm^2/ions are obtained. The former nicely confirms the expected complete wetting of the Au nanoparticles by SiO_2 as experimentally indicated by TEM. From the value of b' an ion-induced viscosity $\eta_r = 1.9 \times 10^{23}$ Pa ions/cm^2 can be extracted for given $\gamma_{SiO_2} = 0.31$ J/m^2 (cf. Ref. 15). In the literature, η_r is reported to depend on the maximum collisional damage S_n due to ion bombardment via a power law[21] $\eta_r \sim S_n^{-1.1}$. In the present case of 200 keV Ar^+ ions bombarding SiO_2, the nuclear damage can be estimated from Monte Carlo simulations [SRIM (Ref. 22)] delivering a maximum value of $S_n = 0.57$ keV/nm, which, according to Ref. 21, translates into $\eta_r = 4 \times 10^{23}$ Pa ions/cm^2 in reasonable agreement with the above value obtained from fitting the data of Fig. 6. Thus, the data presented so far corroborate the state-of-the-art set in Ref. 15 for Pt nanoparticles on SiO_2.

By addressing, however, particle ensembles of *different* starting diameters it will be demonstrated in the following that this present state must be extended significantly. This is most clearly seen by referring to Eq. (8). Changing to the scaled variables $\tilde{\phi} = \phi / R_0$ and $\tilde{h} = h / R_0$ leads to the universal relation given as Eq. (9), which should hold for all particle ensembles alike independent of their starting diameter

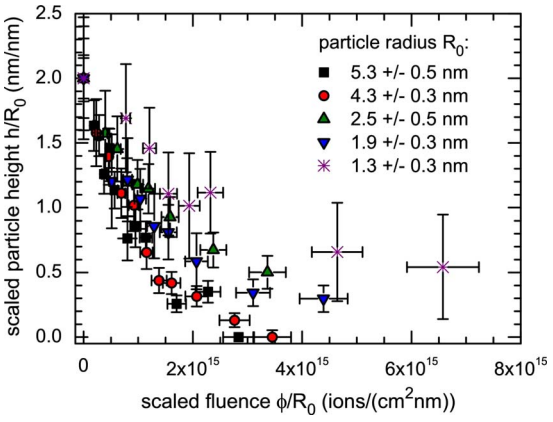

FIG. 7. (Color online) Scaled particle height h/R_0 versus scaled ion fluence ϕ/R_0 for various Au nanoparticle ensembles on top of SiO_2 with different starting radii R_0 as given in the inset.

$$\tilde{\phi}(\tilde{h}) = \frac{1}{b'}(\tilde{h} - 2) - \frac{a}{b'} \ln\left(\frac{\tilde{h} - 2}{a} + 1\right). \tag{9}$$

To test the predicted universal behavior, in Fig. 7 the scaled height is plotted versus the scaled ion fluence for five Au nanoparticle ensembles with starting diameters ranging from 2.6 to 10.6 nm.

The most salient feature in this plot is the fact that all curves, though necessarily starting at $\tilde{h}=2$, fan out for higher ion fluences and by no means collapse onto one common master curve. Equally important and in marked contrast to expectation, smaller particles need larger ion fluences to arrive at a given degree of reduced particle height. Both observations clearly indicate that the standard theoretical description of ion-induced burrowing as given in Ref. 15 is still missing an essential ingredient. One process neglected so far completely is conventional sputtering of nanoparticles leading as well to an ion-induced continuously decreasing particle size. The presence and magnitude of sputtering will be analyzed in Sec. III D.

D. Au nanoparticles on top of (0001)-oriented sapphire irradiated with 200 keV Ar^+: Effect of sputtering

In order to analyze sputtering of Au nanoparticles by 200 keV Ar^+ ions quantitatively, the particles have to be deposited onto a substrate with such a low ion-induced viscosity η_r that the burrowing effect can be neglected. According to the arguments given in Ref. 20, crystalline substrates as opposed to the above thermally prepared amorphous SiO_2 should exhibit strongly reduced η_r values. Experimentally, it turned out that sapphire substrates are especially suited for this purpose. This is demonstrated in Fig. 8, where corresponding TEM images are presented for Au nanoparticles (starting diameter 7.8 nm) on (0001) sapphire after 200 keV Ar^+ irradiation with a fluence of 6.5×10^{15} ions/cm^2. It should be

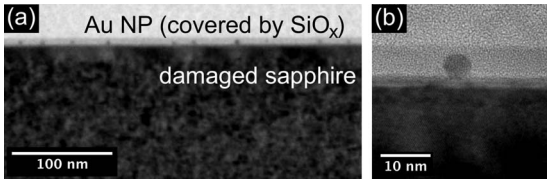

FIG. 8. (a) Bright-field TEM image of Au nanoparticles on top of a sapphire substrate after 200 keV Ar^+-ion irradiation (6.5×10^{15} ions/cm^2). The nanoparticles were embedded in a SiO_x layer after irradiation for TEM preparational reasons. (b) (HR)TEM image of single nanoparticle on top of sapphire. Implantation defects appear as inhomogeneous Bragg contrast of the substrate.

noted that in order to prepare the TEM specimen the nanoparticles had to be embedded into a protecting SiO_x layer since Au nanoparticles do not stick very well to sapphire surfaces in contrary to Si or SiO_2 substrates. This layer, which is clearly visible in Fig. 8(b), of course was evaporated *after* the ion irradiation. At the above fluence corresponding nanoparticles on top of SiO_2 are expected to exhibit a height reduction by a factor of approximately 4. In marked contrast to that expectation, the TEM results in Fig. 8 prove that there is no irradiation-induced burrowing of the nanoparticles. Rather, they stay on top of the sapphire surface [Fig. 8(a)]. Closer inspection [Fig. 8(b)] reveals that the ion bombardment leads to the formation of a damaged surface layer of the substrate with quite a well-defined thickness of about 200 nm reflecting an energy threshold for creating this damage. Though the burrowing effect clearly is absent, the AFM measurements presented in Fig. 9 nevertheless indicate a decrease of the particle height due to ion irradiation with an apparently linear dependence on fluence, which, thus, is attributed to ion-induced erosion, i.e., sputtering. The linear fit, however, fails to deliver the correct starting diameter by extrapolation back to $\phi=0$. Thus, one may suspect that sputtering of nanoparticles leads to a nonlinear sputtering behavior. Indeed, such an idea has been put forward previously and, here, we refer to the quantitative treatment of the problem as given in Ref. 17. Given the damage distribution $F_D(E,\boldsymbol{r},\boldsymbol{r_0})$ describing the radiation damage created by a projectile hitting a spherical nanoparticle at position $\boldsymbol{r_0}$ with energy E, the sputtering yield $Y_0(\boldsymbol{r_0})$ is given by the surface integral

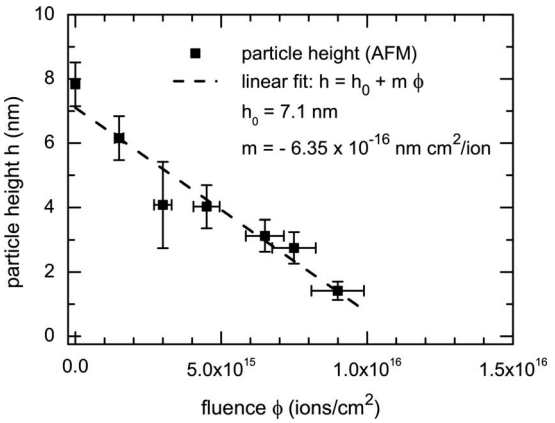

FIG. 9. Ion-induced erosion (sputtering) of Au nanoparticles (starting diameter 7.8 nm) by 200 keV Ar^+ ions as a function of the ion fluence. The experimental data as obtained by AFM height measurements (closed squares) are fitted by a straight line.

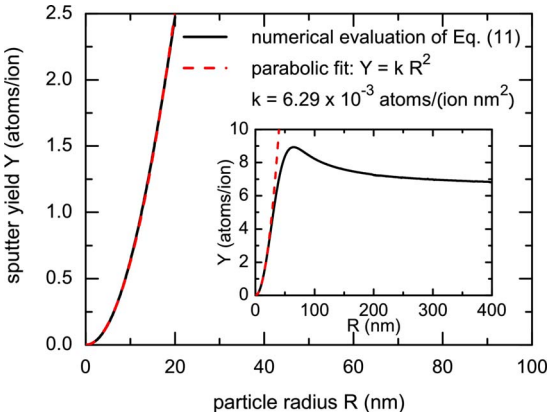

FIG. 10. (Color online) Size-dependent sputter yields of spherical Au nanoparticles due to their bombardment with 200 keV Ar^+ ions. An overview is given in the inset, while the main panel magnifies the behavior for particles with radii below 25 nm. In this range, the calculated results (solid curve) can be fitted by a parabola $Y=kR^2$ (dashed curve).

$$Y_0(\boldsymbol{r}_0) = \Lambda \int_S F_D(E,\boldsymbol{r},\boldsymbol{r_0}) d^2r. \tag{10}$$

Averaging over all $\boldsymbol{r_0}$ on a sphere of radius R delivers

$$Y(R) = \frac{\int Y_0(\boldsymbol{r_0}) d^2r_0}{\int d^2r_0}. \tag{11}$$

From Eq. (10) it is clear that the most important input is the damage distribution F_D, which, however, can be obtained from the Monte Carlo code SRIM (Ref. 22) and approximated by a three-dimensional Gaussian distribution with axial symmetry around the direction of the incoming projectile with its center at the position of the maximum damage R_D and longitudinal and transversal straggling of $\sigma_\parallel$ and $\sigma_\perp$, respectively. In the present case of 200 keV Ar^+ bombarding Au, SRIM delivers $R_D=34$ nm, $\sigma_\parallel=43$ nm, and $\sigma_\perp=45$ nm. Furthermore, Λ in Eq. (10) is adjusted to guarantee that the yield calculated according to Eq. (11) approaches the bulk value Y_b for $R\to\infty$ (here, $Y_b=6.86$ Au atoms per ion according to SRIM). Based on the above Gaussian, Eqs. (10) and (11) were analyzed numerically to derive the radius dependence of the sputtering yield for Au nanoparticles. The result is presented in the inset of Fig. 10 revealing a strong size effect of the sputter yield for diameters below 100 nm while for larger particles the bulk value is approached smoothly. Since our Au nanoparticles are much smaller than the position of the peak in the Y-vs-R curve as given in the inset, the increasing part of that curve for small diameters is magnified and plotted in the main panel of Fig. 10. It turns out that up to a diameter of 20 nm, i.e., within the size range of the present

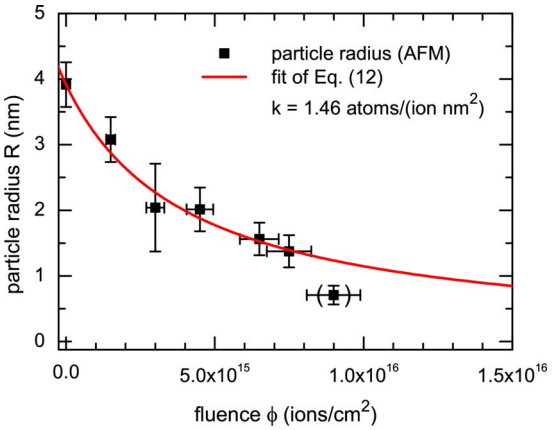

FIG. 11. (Color online) Ion-induced erosion (sputtering) of sapphire-supported Au nanoparticles (starting diameter 7.8 nm) by 200 keV Ar^+ ions as a function of the ion fluence. The experimental data as obtained by AFM height measurements (closed squares) are fitted to Eq. (12) with a parabolic sputter yield $Y(R)=kR^2$.

nanoparticles, the size dependence of the sputter yield can be precisely fitted by a simple parabola $Y(R)=kR^2$. The derived value of $k=0.006\ 29$ atoms/(ion nm^2) delivers a sputter coefficient $Y(3.9\ \text{nm})=0.09$ atoms/ion, which is smaller than the calculated bulk value Y_b by a factor of 75. On the other hand, from the linear fit given in Fig. 9 one obtains a value of $Y(3.9\ \text{nm})=7.5$ atoms/ion close to Y_b. Before discussing this discrepancy, we use the general size dependence $Y(R)$ to extract the experimentally accessible relation between the particle radius and the ion fluence $R(\phi)$. Assuming a size-independent number density n, one obtains

$$\phi(R) = -4n\int_{R_0}^{R}\frac{dR'}{Y(R')}. \tag{12}$$

While for a size-independent sputter yield Y, Eq. (12) immediately leads to the standard linear relation $R(\phi)=R_0-Y\phi/(4n)$, the above parabolic dependence $Y(R)=kR^2$ gives $R(\phi)=(4nR_0)/(4n+kR_0\phi)$. For the Au nanoparticles on sapphire (starting diameter 7.8 nm) irradiated with 200 keV Ar^+ ions this latter relation is tested in Fig. 11. If the experimental data point obtained for the highest ion fluence, i.e., for the smallest particle, is excluded, excellent agreement is found with a fit parameter $k=1.46$ atoms/(ion nm^2). Especially, in contrast to the linear fit in Fig. 9, the starting diameter for $\phi=0$ is correctly included by the nonlinear description. The k value, however, similar to the sputter yields given above, is by approximately 2 orders of magnitude larger than what is expected from theory (cf. Fig. 10). To resolve this discrepancy one should note that the theoretical approach is for nonsupported nanoparticles, while the ion bombardment involves the substrate as well. For instance, collision cascades moving backward within the substrate in close vicinity to a supported nanoparticle may contribute to the particle sputtering while not considered in theory. Thus, at present, though the experimental data certainly are not sufficient to prove or disprove a quantitative relation such as $Y(R)=kR^2$, the results of this section clearly demonstrate that sputtering of the Au nanoparticles cannot be neglected when describing the ion-induced burrowing process. Additionally, these results may suggest a size dependence of the sputtering yield. Finally, even the neglected data point in Fig. 11 for particles with $R<1$ nm exhibiting a strongly enhanced sputter yield could be explained by a significantly increased vapor pressure of these small particles due to their extreme curvature ("Kelvin effect").[23] Such an increased vapor pressure translates into a decreased surface binding energy, which immediately leads to an enhancement of the sputter yield, i.e., to a deviation of the experimental particle radius from the fitted behavior toward smaller values. It is also worth noting that the high degree of hexagonal order of the nanoparticle ensembles (cf. Fig. 1) allows testing for completely removed particles due to the ion bombardment. However, no such event was found within our AFM statistics indicating that spikes triggered within a nanoparticle by 200 keV Ar^+ irradiation and leading to complete particle destruction must be rare.

E. Au nanoparticles on top of silicon oxide irradiated with 200 keV Ar^+: Combination of ion-induced burrowing and sputtering

To include sputtering in the theoretical description of the burrowing effect, one starts with the relation $2R(\phi)=h(\phi)+z(\phi)$, but now taking the decrease of the radius due to sputtering explicitly into account. Thus, the previous $dh/d\phi$ has to be complemented by $2dR/d\phi$ resulting in

$$\frac{dh}{d\phi} = b'\frac{h+(a-2)R}{h-2R} + 2\frac{dR}{d\phi}. \tag{13}$$

Consequently, sputtering is all contained in the second term of Eq. (13), which in the case of a constant size-independent yield reads $dR/d\phi=-Y/(4n)$. Comparison to the universal Eq. (9) leads to the conclusion that substituting $dR/d\phi$ together with $R(\phi)=R_0-Y\phi/(4n)$ back into Eq. (13) again delivers such a universal expression $\tilde{\phi}$ vs $\tilde{h}$ predicting a mastercurve for all particle ensembles independent of their starting diameter as opposed to the experimental observation (cf. Fig. 7). Thus, in order to make Eq. (13) compatible with the experimentally found fanning curves of Fig. 9, a radius-dependent term $dR/d\phi$, i.e., a size-dependent sputter yield $Y(R)$, is necessary. Based on the approximate relation $Y=kR^2$, one obtains $dR/d\phi=-AR_0^2/(1+AR_0\phi)^2$, with $A=k/(4n)$. With these expressions substituted into Eq. (13), the final equation can be extracted in scaled variables $\tilde{\phi}=\phi/R_0$ and $\tilde{h}=h/R_0$,

$$\frac{d\tilde{h}}{d\tilde{\phi}} = b'\frac{\tilde{h}+\dfrac{(a-2)}{1+AR_0^2\tilde{\phi}}}{\tilde{h}-\dfrac{2}{1+AR_0^2\tilde{\phi}}} - \frac{2AR_0^2}{(1+AR_0^2\tilde{\phi})^2}. \tag{14}$$

Here, the starting radius acts as a group parameter delivering an individual curve for each parameter as in the experiment. Equation (14), however, has to be integrated numerically to arrive at $h(\phi)$, the quantity immediately comparable to experiment. Such a comparison is presented in Fig. 12. Here, three theoretical models are tested: the thermodynamically

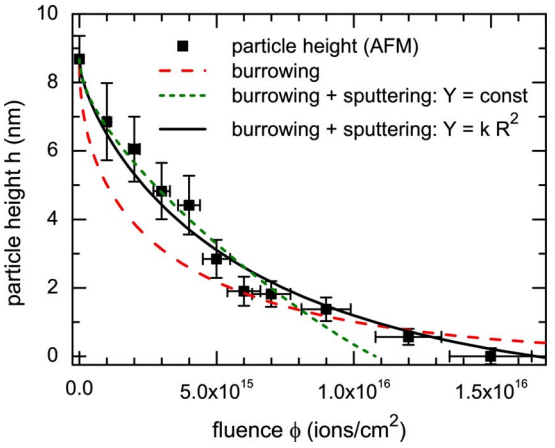

FIG. 12. (Color online) Modeling of ion-induced (200 keV Ar^+) burrowing of Au nanoparticles (starting diameter 8.6 nm) on top of SiO_2 including sputtering as given in the inset.

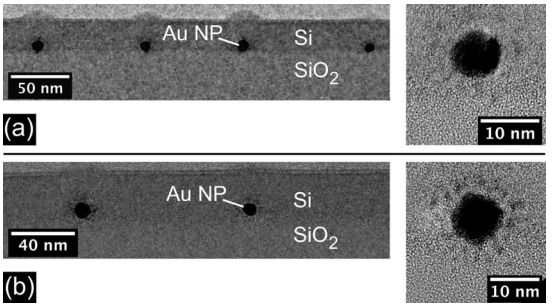

FIG. 13. Au nanoparticles on top of SiO_2 covered by Si prior to ion irradiation: bright-field TEM images (left) and (HR)TEM images of single particles (right) at two different ion fluences: (a) 4×10^{15} ions/cm^2 and (b) 6×10^{15} ions/cm^2. The higher fluence does not change the position of the particles but results in a more pronounced effect of sputtering.

driven ion-induced burrowing effect (dashed curve, same as in Fig. 6), burrowing effect combined with sputtering at a size-independent sputter coefficient (dotted curve), and burrowing effect combined with size-dependent sputtering according to $Y=kR^2$ (solid curve). The results of Fig. 12 convincingly prove that sputtering has to be included in order to obtain satisfactory agreement between the model description and the experiment. One step further, it appears that a size-independent sputter yield delivers an excellent approximation for larger particles at the beginning of their irradiation while a size-dependent yield is more appropriate for smaller particles, i.e., for larger ion fluences. It is worth noting that keeping the fit parameters $a=2$, $b'=1.1\times10^{-16}$ nm cm^2/ion, $k=0.63$, and $\eta_r=1.8\times10^{24}$ Pa ions/cm^2 fixed as extracted from Fig. 12, delivers an excellent description for all ensembles with different starting radii presented in Fig. 7 except for the particles with $R_0=1.9$ nm. In that case, the parameters b' and k had to be changed to $b'=2.6\times10^{-16}$ nm cm^2/ion and $k=0.46$ in order to improve agreement.

Thus, at this point it can be concluded that adding a size-dependent sputtering to the thermodynamically driven ion-induced burrowing effect immediately resolves the problem of nonuniversal $\tilde{\phi}$-vs-$\tilde{h}$ curves as observed experimentally. Furthermore, the fit parameters extracted from such a description of various irradiated particle ensembles are well within the range expected from previous work. Since, however, the fits turn out to be rather insensitive to the value of k describing the sputtering yield and, at least partly, can be compensated by a change of parameter b', the detailed size dependence of sputtering still remains an open question.

F. Au nanoparticles on top of silicon oxide covered by silicon prior to irradiation with 200 keV Ar^+: Support of thermodynamic driving forces

According to the introductory Eq. (1) the thermodynamic driving force for the burrowing effect should be significantly reduced if the particles are completely covered before the ion irradiation by a second material different from SiO_2. In that case, the surface energy of the particle γ_p should be substituted by the interface energy $\gamma_{p,m}$ between the particle and the second material. To test this expectation, Au nanoparticles as before on top of SiO_2 were completely embedded in a 40 nm thick evaporated Si layer and, afterwards, irradiated with 200 keV Ar^+ ions. As proven by the TEM images presented in Fig. 13, after irradiating a fluence of 4×10^{15} ions/cm^2, which for uncovered Au nanoparticles of similar size leads to a significant burrowing effect (cf. Fig. 7), the Si-embedded nanoparticles still are localized at the SiO_2 surface. Even increasing the fluence further to 6×10^{15} ions/cm^2 did not result in burying the particles. Rather, the particles start being dissolved by the ion bombardment similar to the behavior of uncovered particles which were buried by ion irradiation first and then exposed to further bombardment [cf. Fig. 2(d)]. Similar results have been reported previously by Heinig *et al.*[24] and Rizza *et al.*[25] for Au nanoparticles under ion irradiation within a SiO_x matrix. Since, on the other hand, the thin covering Si layer does not significantly change the energy and flux of the projectiles at the substrate surface supporting the nanoparticles, the local ion-induced kinetics dominating the local viscosity should closely compare to the bombardment of uncovered particles. Thus, the images of Fig. 13 provide clear evidence that the additional thermodynamic driving force related to a contrast in surface energies is necessary for obtaining an ion-induced particle burrowing. The question remains as to the influence of the local defect production on the burrowing effect. This will be addressed next.

G. Au nanoparticles on top of silicon oxide irradiated with 200 keV Xe^+: Influence of projectile on the ion-induced burrowing effect

As mentioned already in Sec. III C, the kinetics of the ion-induced burrowing effect as expressed by the viscosity η_r is expected to depend on the defect production or nuclear energy loss of the projectiles close to the substrate surface. According to SRIM simulations, for 200 keV Ar^+ ions one obtains a nuclear damage expressed in terms of displacements of target atoms per depth interval and projectile of 0.28 displacements per target atom (dpa)/Å, while the cor-

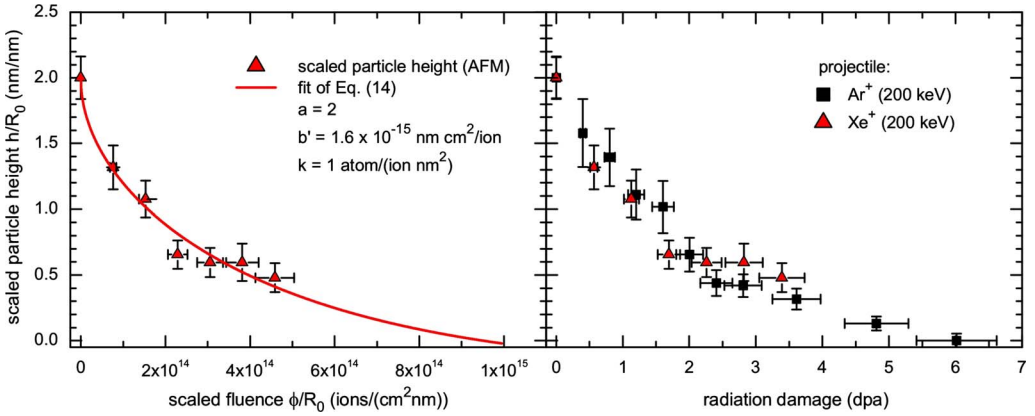

FIG. 14. (Color online) Ion-induced burrowing of Au nanoparticles (starting radius 3.8 nm) on top of SiO_2 induced by 200 keV Xe^+. Left panel: scaled particle height versus scaled ion fluence and fit according to Eq. (14). Right panel: scaled particle height versus displacements per atom as calculated from SRIM (Ref. 22) including results for Ar^+ (200 keV) irradiation of Au particles (starting radius 4.3 nm).

responding value for 200 keV Xe^+ is 1.35 dpa/Å. In both cases an average is taken over the first 10 nm within the SiO_2 substrate. A similar difference is found for the sputtering coefficients with $Y_{Ar}=0.84$ atoms/ion and $Y_{Xe}=3.32$ atoms/ion for SiO_2. In a first step, in Fig. 14(a) the ion-induced burrowing effect of Au nanoparticles (starting radius 3.8 nm) is demonstrated in scaled units $\tilde{\phi}$ and $\tilde{h}$ for 200 keV Xe^+ irradiation. The experimental data are again analyzed by fitting to Eq. (14), i.e., a size-dependent sputtering is included. The resulting solid curve delivers an excellent description of the experiment with the parameters $a=2$ and $b'=1.6\times10^{-15}$ nm cm^2/ion leading to $\eta_r=1.3\times10^{23}$ Pa ions/cm^2 and $k=1$ atom/(ion nm^2) with the latter parameter reflecting the higher sputtering coefficient of Xe as compared to Ar projectiles. Also the value of η_r is consistent with the predictions given in Ref. 21 for a nuclear energy loss of 2.3 keV/nm as found by SRIM for 200 keV Xe^+ ions in SiO_2. In order to test whether the burrowing effect can be scaled for different projectiles by switching from fluence to dpa as variable, in panel (b) of Fig. 14 the data of panel (a) are correspondingly replotted together with results for an Ar^+ irradiation of Au nanoparticles of comparable starting size. The most notable feature here is that the curves for the two different projectiles, which in terms of ion fluences are completely split, now fall on top of each other as a consequence of the dpa scaling. This is in accordance with the notion that the ion-induced viscosity of the substrate η_r and the sputter yield of the nanoparticles both are proportional to the nuclear damage provided by a bombarding projectile.

IV. CONCLUSIONS

Based on preparational progress allowing fabrication of well-ordered ensembles of Au nanoparticles exhibiting narrow size distributions on top of SiO_2 substrates, the ion-induced burrowing effect could be quantitatively analyzed by exploiting sufficient statistics delivered by AFM measurements on such ion-irradiated ensembles. Three main conclusions can be drawn from the results presented here:

(i) Thermodynamic driving forces related to the surface and interface energies of particle and substrate are necessary to arrive at an observable ion-induced burrowing effect. This prerequisite must be accompanied by a sufficient irradiation-induced viscosity of the substrate, which was found to scale with the nuclear damage produced by a projectile close to the substrate surface.

(ii) In order to describe the burrowing effect quantitatively, in addition to the thermodynamically driven part sputtering has to be included. One step further, to obtain individual burrowing curves even in scaled variables for each particle ensemble with a given starting size as observed experimentally, a size-dependent sputtering coefficient has to be chosen.

(iii) The burrowing curves as experimentally obtained for Ar^+ and Xe^+ irradiations can be scaled on top of each other by a description in terms of dpa rather than ion fluence.

ACKNOWLEDGMENTS

The financial support by DFG via Contracts No. SFB 569 and No. GRK 328 as well as by Landesstiftung Baden-Württemberg via network "Functional Nanostructures" are gratefully acknowledged. The authors thank Balati Kuerbanjiang for experimental assistance in performing AFM measurements as well as Masaki Ozawa for performing part of the TEM measurements and Sabine Grözinger for TEM sample preparation. The authors are also grateful to Paul Walther (ZE Electron Microscopy, Ulm University) and Katharina Landfester (OC III, Ulm University) for providing access to their SEM and AFM, respectively.

*Present address: DR. JOHANNES HEIDENHAIN GmbH, 83301 Traunreut, Germany.
†paul.ziemann@uni-ulm.de

[1] M. Nastasi and J. W. Mayer, *Ion Implantation and Synthesis of Materials* (Springer-Verlag, Berlin, 2006).
[2] *Proceedings of the 15th International Conference on Ion Beam Modification of Materials*, Taormina Italy, (2006), edited by M. G. Grimaldi, G. Impellizzeri, S. Mirabella, and L. Romana [Nucl. Instrum. Methods Phys. Res. B **257**, 1 (2007)].
[3] M. Strobel, K.-H. Heinig, W. Möller, A. Meldrum, D. S. Zhou, C. W. White, and R. A. Zuhr, Nucl. Instrum. Methods Phys. Res. B **147**, 343 (1999).
[4] A. Miotello, G. De Marchi, G. Mattei, P. Mazzoldi, and C. Sada, Phys. Rev. B **63**, 075409 (2001).
[5] U. Kaiser, D. A. Muller, J. L. Grazul, A. Chuvilin, and M. Kawasaki, Nature Mater. **1**, 102 (2002).
[6] J. Biskupek, U. Kaiser, H. Lichte, A. Lenk, T. Gemming, G. Pasold, and W. Witthuhn, J. Magn. Magn. Mater. **293**, 924 (2005).
[7] S. Gilb, M. Arenz, and U. Heiz, Mater. Today **9**, 48 (2006).
[8] S. Krishnamoorthy, C. Hinderling, and H. Heinzelmann, Mater. Today **9**, 40 (2006).
[9] *Nanoparticles: From Theory to Application*, edited by G. Schmid (Wiley-VCH, Weinheim, 2004), Vol. 1.
[10] S. Gilb, K. Hartl, A. Kartouzian, J. Peter, U. Heiz, H.-G. Boyen, and P. Ziemann, Eur. Phys. J. D **45**, 501 (2007).
[11] A. Ethirajan, U. Wiedwald, H.-G. Boyen, B. Kern, L. Han, A. Klimmer, F. Weigl, G. Kästle, P. Ziemann, K. Fauth *et al.*, Adv. Mater. (Weinheim, Ger.) **19**, 406 (2007).
[12] G. Kästle, H.-G. Boyen, F. Weigl, G. Lengl, T. Herzog, P. Ziemann, S. Riethmüller, O. Mayer, C. Hartmann, J. P. Spatz *et al.*, Adv. Funct. Mater. **13**, 853 (2003).
[13] H.-G. Boyen, G. Kästle, K. Zürn, T. Herzog, F. Weigl, P. Ziemann, O. Mayer, C. Jerome, M. Möller, J. P. Spatz *et al.*, Adv. Funct. Mater. **13**, 359 (2003).
[14] R. Kissel and H. M. Urbassek, Nucl. Instrum. Methods Phys. Res. B **180**, 293 (2001).
[15] X. Hu, D. G. Cahill, and R. S. Averback, J. Appl. Phys. **92**, 3995 (2002).
[16] J. Biskupek, U. Kaiser, and F. Falk, J. Electron Microsc. **57**, 83 (2008).
[17] T. T. Järvi, J. A. Pakarinen, A. Kuronen, and K. Nordlund, EPL **82**, 26002 (2008).
[18] J. Bansmann, S. Kielbassa, H. Hoster, F. Weigl, H.-G. Boyen, U. Wiedwald, P. Ziemann, and R. J. Behm, Langmuir **23**, 10150 (2007).
[19] I. Horcas, R. Fernández, J. M. Gómez-Rodríguez, J. Colchero, J. Gómez-Herrero, and A. M. Baro, Rev. Sci. Instrum. **78**, 013705 (2007).
[20] S. G. Mayr, Y. Ashkenazy, K. Albe, and R. S. Averback, Phys. Rev. Lett. **90**, 055505 (2003).
[21] E. Snoeks, T. Weber, A. Cacciato, and A. Polman, J. Appl. Phys. **78**, 4723 (1995).
[22] J. P. Biersack and L. G. Haggmark, Nucl. Instrum. Methods **174**, 257 (1980).
[23] F. Weigl, B. Koslowski, and P. Ziemann, Surf. Sci. **602**, 3714 (2008).
[24] K. Heinig, T. Müller, B. Schmidt, M. Strobel, and W. Möller, Appl. Phys. A: Mater. Sci. Process. **77**, 17 (2003).
[25] G. Rizza, H. Cheverry, T. Gacoin, A. Lamasson, and S. Henry, J. Appl. Phys. **101**, 014321 (2007).